Taylor & Francis
Taylor & Francis Group

Numerical Heat Transfer, Part A: Applications

An International Journal of Computation and Methodology

Numerical modeling and experimental investigation of a prismatic battery subjected to water cooling

S. Panchal, R. Khasow, I. Dincer, M. Agelin-Chaab, R. Fraser & M. Fowler

Published online: 10 Mar 2017.

Submit your article to this journal

View related articles

View Crossmark data

Taylor & Francis
Taylor & Francis Group

Numerical modeling and experimental investigation of a prismatic battery subjected to water cooling

S. Panchal[a], R. Khasow[a], I. Dincer[a], M. Agelin-Chaab[a], R. Fraser[b], and M. Fowler[c]

[a]Department of Automotive, Mechanical & Manufacturing Engineering, Faculty of Engineering & Applied Science, University of Ontario Institute of Technology, Oshawa, Ontario, Canada; [b]Mechanical and Mechatronic Engineering Department, University of Waterloo, Waterloo, Ontario, Canada; [c]Chemical Engineering Departments, University of Waterloo, Waterloo, Ontario, Canada

ABSTRACT

In this paper, a numerical model using ANSYS Fluent for a minichannel cold plate is developed for water-cooled LiFePO$_4$ battery. The temperature and velocity distributions are investigated using experimental and computational approach at different C-rates and boundary conditions (BCs). In this regard, a battery thermal management system (BTMS) with water cooling is designed and developed for a pouch-type LiFePO$_4$ battery using dual cold plates placed one on top and the other at the bottom of a battery. For these tasks, the battery is discharged at high discharge rates of 3C (60 A) and 4C (80 A) and with various BCs of 5°C, 15°C, and 25°C with water cooling in order to provide quantitative data regarding the thermal behavior of lithium-ion batteries. Computationally, a high-fidelity computational fluid dynamics (CFD) model was also developed for a minichannel cold plate, and the simulated data are then validated with the experimental data for temperature profiles. The present results show that increased discharge rates (between 3C and 4C) and increased operating temperature or bath temperature (between 5°C, 15°C, and 25°C) result in increased temperature at cold plates as experimentally measured. Furthermore, the sensors nearest the electrodes (anode and cathode) measured the higher temperatures than the sensors located at the center of the battery surface.

1. Introduction

Currently, the automotive industry is rapidly moving toward electric vehicles (EVs), hybrid electric vehicles (HEVs), plug-in hybrid electric vehicles (PHEVs), and fuel cell vehicles (FCVs) to alleviate the environmental issues. Currently, lithium-ion batteries are gaining widespread acceptance in the development of EVs, HEVs, and PHEVs [1]. Their extensive usage is due to: 1) high specific energy and power densities [2, 3]; 2) high nominal voltage and low self-discharge rate [4]; and 3) long cycle-life and no memory effect [5]. The optimal operation of lithium-ion batteries, in terms of both efficiency and cycling life, depends critically on their thermal management [6, 7]. A battery thermal management system (BTMS) is required to secure the desired performance of a battery or battery pack in a low-temperature environment and the desired lifetime in a high-temperature environment. In addition, the temperature, an important factor, affects several aspects of a lithium-ion battery, including the thermal and electrochemical behaviors, and ultimately affects the vehicle performance

CONTACT S. Panchal ✉ satyam.panchal@uoit.ca; satyam.panchal@uwaterloo.ca 🖃 Department of Automotive, Mechanical & Manufacturing Engineering, Faculty of Engineering & Applied Science, University of Ontario Institute of Technology, 2000 Simcoe Street North, Oshawa, Ontario, Canada, L1H 7K4.
Color versions of one or more of the figures in the article can be found online at www.tandfonline.com/unht.

Nomenclature

C	cell voltage or cell potential [V]	$\vec{V}$	average velocity [m/s]
$C_{1\varepsilon}$	model constants	ω	turbulent eddy frequency [1/s]
$C_{2\varepsilon}$	model constants	y^+	enhanced wall treatment
$C_{3\varepsilon}$	model constants	Y_M	the contribution of the fluctuating dilatation
C_μ	constant		in compressible turbulence to the overall
G_k	generation of turbulence kinetic energy		dissipation rate
	due to the mean velocity gradients		
G_b	generation of turbulence kinetic energy	**Greek Symbols**	
	due to buoyancy	∇	gradient operator
I	current [A]	μ	viscosity [Pas]
k	turbulent kinetic energy [J]	μ_t	turbulent (or eddy) viscosity
P	pressure [Pa]	λ	Reynold's stress
Pr	Prandtl number	σ_k	turbulent Prandtl numbers for k
Pr_t	turbulent Prandtl number	ε_k	turbulent Prandtl numbers for ε
Re	Reynold's number		
S_k	user-defined source terms	**Subscripts**	
S_ε	user-defined source terms	max	maximum
T	temperature [°C or K]		
t	time [s]	**Superscripts**	
V	speed [m/s]	°	degree
		+	Related to wall treatment

and cost of the cycle life [8, 9]. A typical range of temperature is between 20°C and 40°C [10], and an extended range is between −10°C and +50°C for tolerable operation [11, 12] for lithium-ion batteries. There are different methods of BTMS that include: i) air cooling and ii) water cooling. Air cooling has attracted the attention of many researchers because of its simplicity [13] and light weight. Water cooling is a more efficient method because of its ability to absorb more heat, compared with air cooling, and it occupies less volume, but brings more complexities as well as high cost and weight [14–16]. In addition, because of the low thermal conductivity of air [17], very high velocity of air is necessary to sufficiently cool the lithium-ion batteries using active cooling methods [18, 19]. On the other hand, liquid cooling gives better cooling compared with air cooling due to its high thermal conductivities [20].

There are various papers in the open literature available for battery thermal modeling, using different approaches such as artificial neural network [21–23], finite element model (FEM) [24, 25], lumped parameter model (LPM) [6], linear parameter varying (LPV) model [26], partial differential equation (PDE) model [27], and computational fluid dynamics (CFD) model [8, 16, 28–33]. A liquid cooling system with two cold plates placed one on the top and the other at the bottom of the battery removes heat generated within the lithium-ion battery using a metal thin-wall structure with several channels. This kind of system is able to reduce the operating temperature, which maintains the uniform temperature distributions. Lin, Xu, Chang, and Liu also developed a three-dimensional numerical model of the battery pack with passive TMS using ANSYS Fluent. Their experimental results showed that phase change material (PCM) cooling significantly reduced the battery temperature rise during short-time intense use. It was also found that temperature uniformity across the module deteriorates with the increase of both discharge time and current rates. Rao, Wang, and Huang [34] developed a three-dimensional battery thermal model using ANSYS Fluent and studied the effect of various influencing factors, especially mass flow rate of water, phase change temperature, and thermal conductivity of PCM. Their results showed that the liquid volume fraction of PCM was greatly influenced by the thermal conductivity and the phase change temperature of PCM. The increasing number of channels results in a decrease of the maximum temperature (Tmax) and maximum temperature difference (ΔT) of battery packs. Anderson, Devost, Pakdee, and Krishnamoorthy [35] also studied heat transfer and fluid flow simulation of a novel heat exchanger/cold plate fabricated from k-core high thermal conductivity material in order to realize the thermal control system

hardware design for applications to very large power density ($\sim$1kW/m^2) electronics packaging scenarios. In another study, Ye et al. [5] proposed an optimized heat pipe thermal management system (HPTMS) for fast-charging lithium-ion battery cell/pack. A numerical model was developed and validated with the experimental results. Then the model was employed to investigate the thermal performance of the HPTMS under steady-state and transient conditions. Lastly, Huo et al. [36] also designed a minichannel cold plate-based BTMS to cool a rectangular lithium-ion battery. They studied the effects of number of channels, flow direction, inlet mass flow rate, and ambient temperature on temperature rise and distribution of the battery during the discharge process, and found that the maximum temperature of the battery decreases with increase in the number of channels and inlet mass flow rate.

The performance of a liquid cooling-based BTMS with dual cold plates depends on various factors like mass flow rate of the liquid and ambient temperature or battery casing temperature. In this paper, a minichannel cold plate-based BTMS was designed and comprehensive investigation and simulation were conducted on the lithium-ion battery performance under different constant current discharge rates of 3C and 4C, and boundary conditions (BCs) of 5°C, 15°C, and 25°C for water cooling and 22°C for air cooling, and the performance was evaluated. To the best of the authors' knowledge, no similar studies on the thermal testing of minichannel cold plates placed on prismatic lithium-ion battery have been reported in the open literature.

2. Experimental study

In this section, the experimental details are provided through the experimental setup, battery, cold plate setup, thermocouple locations, thermal data acquisition system, battery cooling system, and experimental plan and procedure.

2.1. Experimental setup

The battery and cold plate setup is shown in Figure 1. Two commercial available cold plates were used for this experimental work to remove the heat generated from the lithium-ion battery during discharge. One cold plate was placed on the top surface of the battery and the other cold plate was placed on the bottom surface of the battery. The plates are characterized as having a single flow channel with one inlet and one outlet placed on both the top and bottom of the battery. The single

Figure 1. Experimental setup showing the battery and cold plates.

Table 1. Experimental test parameters.

Cooling type	Boundary temperature [°C]	Charge rate	Discharge rate
Water cooling	5	1C	3C, 4C
	15	1C	3C, 4C
	25	1C	3C, 4C
Air cooling	~22	1C	3C, 4C

flow channel runs down the length of the plate before turning back on itself, stepping one channel width across the plate with each turn. This flow pattern results in a thermal profile where the coolant temperature gradient is the largest across the width of the plate. A prismatic lithium-ion battery used in EVs was selected for this work. It was chosen because it is suitable as a basic block for a large battery pack foreseen for commercial automotive vehicle applications. The prismatic battery has the following specifications according to the manufacturer's data sheet: (i) a nominal capacity of 20 Ah; (ii) LiFePO$_4$ as the cathode material (LFP), (iii) graphite as the anode material, (iv) a nominal voltage of 3.3 V, (v) a mass of 496 g, (vi) an internal resistance of 0.5 mΩ, (vii) dimensions of 7.25 mm × 160 mm × 227 mm (as thickness × width × height), and (viii) operating temperature range of −30°C to 55°C. For an ambient air cooling temperature, the lithium-ion battery was placed in a vertical position on a stand inside the lab where the temperature was 22°C. Total nineteen thermocouples were used for this experimental work, out of which, ten T-type thermocouples were placed on the surface of the battery. Three additional thermocouples were also pasted: the first one near the cathode, the second near the anode, and the third near the midbody. Two more thermocouples were used to measure the tab (electrode or current collector) temperature values during different discharge rates at various BCs. Finally, four K-type thermocouples were used to measure the water inlet and outlet temperatures for the top and bottom cold plates.

2.2. Experimental procedure and measurement

In the experimental measurements, three different coolant temperatures or BCs were used for the water cooling method: 5°C, 15°C, and 25°C, and for the air cooling method: 22°C. Two different discharge rates (constant current) were selected: 3C and 4C. The charge rate (constant current–constant voltage) is 1C. The experimental plan is shown in Table 1. The following procedure was performed. i) The isothermal water fluid bath and pump were turned on, two hours prior to beginning the cycling, in order to bring the battery, bath, and compression rig to a steady-state temperature. The valves leading to the cold plates were observed and set to open. The isothermal water fluid bath was set to the desired cooling temperature or BCs of 5°C, 15°C, and 25°C for the test. ii) The LabVIEW code for the charge/discharge stand (battery electrical data collection) was loaded and the relevant test parameters, such as charge current, discharge current, charge voltage, discharge voltage, and sampling rate, were input to the program. iii) The thermal data acquisition PC (Computer-2) and Keithly 2700 were turned on and allowed to initialize. On the PC, the Excel Link recording software was prepared for data acquisition such as surface temperature and water inlet and outlet temperatures at the top and bottom of the cold plate.

3. Numerical modeling

3.1. Governing equations

The water flow in the cold plates is turbulent and therefore the flow was modeled using the Reynolds-Averaged Navier–Stokes Equations (RANS). Since the temperature field is also of interest, the Reynolds-Averaged Energy equation was solved as well. The governing equations are:

$$\nabla \cdot \vec{V} = 0 \tag{1}$$

$$\rho \left[\frac{\partial \overline{V}}{\partial t} + (\vec{V} \cdot \nabla \overline{V})\right] = -\nabla \overline{p} + (\mu \nabla^2 \overline{V} - \lambda) \tag{2}$$

$$\frac{\partial \rho \overline{T}}{\partial t} + \rho \vec{V} \nabla T = \nabla \cdot \left[\left(\frac{\mu}{Pr} + \frac{\mu_t}{Pr_t}\right)\nabla \overline{T}\right] \tag{3}$$

where ∇ is the gradient operator, $\vec{V}$ is the average velocity (m/s), V is the speed (m/s), ρ is the density (kg/m^3), P is the pressure (Pa), μ is the viscosity (Pas), λ is the gradient of Reynold's stress, Pr is the Prandtl number, and Pr_t is the turbulent Prandtl number.

Since the flow in the problem is assumed to be turbulent, an appropriate turbulence model is required. In this study, the standard k-ε turbulence model was used given the robustness of the model, reasonable accuracy for a wide range of flows, and its proven capability in heat transfer and flow analysis. The equations in ANSYS Fluent for turbulent kinetic energy and rate of dissipation are as follows [37]:

$$\frac{\partial \rho k}{\partial t} + \nabla * \left[\rho \vec{V} k\right] = \nabla * \left[\left(\mu + \frac{\mu_t}{\sigma_k}\right)\nabla k\right] + G_k + G_b - \rho \varepsilon - Y_M + S_k \tag{4}$$

$$\frac{\partial \rho \varepsilon}{\partial t} + \nabla * \left[\rho \vec{V} \varepsilon\right] = \nabla * \left[\left(\mu + \frac{\mu_t}{\varepsilon_k}\right)\nabla \varepsilon\right] + C_{1\varepsilon}\frac{\varepsilon}{k}(G_k + C_{3\varepsilon}G_b) - C_{2\varepsilon}\,\rho\,\frac{\varepsilon^2}{k} + S_\varepsilon \tag{5}$$

where $C_{1\varepsilon}$, $C_{2\varepsilon}$, $C_{3\varepsilon}$ are the model constants, σ_k and ε_k are the turbulent Prandtl numbers for k and ε. G_k represents the generation of turbulence kinetic energy due to the mean velocity gradients, G_b is the generation of turbulence kinetic energy due to buoyancy. Y_M represents the contribution of the fluctuating dilatation in compressible turbulence to the overall dissipation rate. S_k and S_ε are user-defined source terms. The turbulent (or eddy) viscosity is computed by combining k and ε as follows:

$$\mu_t = C_\mu\,\rho\,\frac{k^2}{\varepsilon} \tag{6}$$

where C_μ is a constant. The ANSYS Fluent was used in this study because of its flexibility and availability. Starting from an initial condition, the solution strides towards a steady-state. Convergence was judged against the normalized continuity, momentum and energy residuals and is considered converged when these residuals have been reduced to 1×10^{-6}.

3.2. Geometry and BCs

The full geometry with the top and bottom cold plates along with the lithium-ion battery in NX 8.5 is depicted in Figure 2. In a CFD simulation, the term "wall" refers to any solid surface that the flow cannot penetrate and thus includes the walls, the floor, ceiling, and surfaces of the test battery. The following is a summary of the BCs that have been applied to the model based on the experimental study. The plate temperature is kept constant. The inlet velocity is specified to obtain the desired value of Reynolds number. The following parameters were selected for model development: 1) viscous model: $R_e = 8.7 \times 10^3$; 2) the wall distance was 1.1×10^{-4}; 3) $C_1 = 1.44$; 4) $C_2 = 1.92$; 5) TKE Prandtl number = 1; 6) TDR Prandtl number = 1.3; 7) energy Prandtl number = 0.85; 8) wall Prandtl number = 0.85; 9) in the turbulent specification method: turbulent intensity of 5% and turbulent viscosity ratio of 10; 10) solver: type : pressure-based; time: steady state; velocity formulation: absolute velocity; 11) residuals convergence variables: X-velocity, Y-velocity, Z-velocity, energy, k-epsilon, continuity equation; 12) wall treatment ($y^+ = 5$); 13) number of elements: approximately 20 million; 14) method for meshing: unstructured tetrahedral with the prism wall layers; 15) convergent criteria: 0.000001 residuals; 16) 1st or 2nd order: 2nd order; 17) type of flow: turbulent. Finally, the following
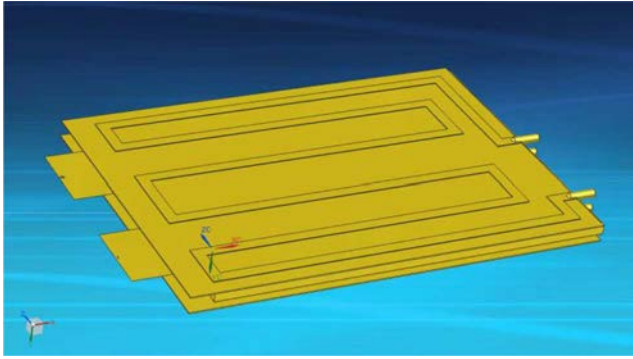
Figure 2. Top and bottom cold plates with lithium-ion battery in NX 8.5.

assumptions were made: 1) symmetry about the center of the battery, and 2) adiabatic on the outside surface of the cooling plate.

3.3. Mesh generation and grid independence study

The meshing of the domain is a very important step since various meshing parameters, such as the number of nodes and the shape of the elements, have a significant impact on the accuracy of the results and the numerical behavior of the solution. A fine unstructured tetrahedral mesh was generated using ANSYS ICEM to resolve all flow features of interest. The overall meshing generated within the assembly is shown in Figure 3. The flow along the various surfaces in the space is resolved by using a finer mesh size around those obstacles, while the boundary layers along all surfaces are resolved by clustering three layers of prismatic elements near the walls. The prismatic layers are also adjusted such that the first node is 0.1 mm away from the wall. This wall node spacing yields a dimensionless wall distance of $y^+ \sim 1$, where y^+ was chosen to be 5. This value is consistent with the recommended value for near-wall flows, while being closer to the acceptable values for the standard k-ε turbulence model. It trades off extreme resolution with lower y^+ values but still maintaining some approximation of the boundary layer. The total number of elements used for the mesh is approximately 20 million. It was ensured that the numerical results are mesh-independent by
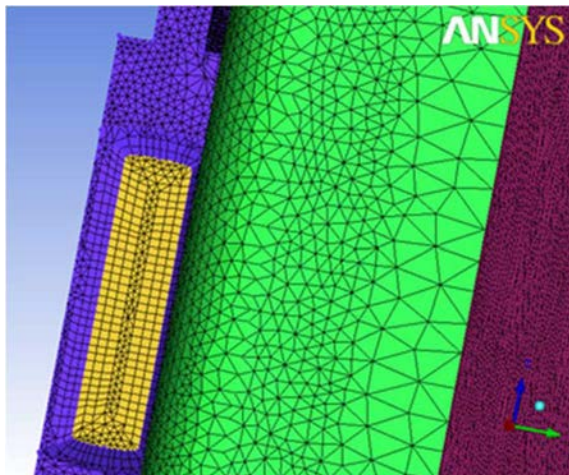
Figure 3. Meshing in ICEM-CFD.

Table 2. Grid independence data for temperature contours.

[Data] Chart Count	20 million cells 50% Larger Temperature [K]	33 million cells Nominal Temperature [K]	40 million cells Next Inlet Channel Finer (0.2 mm) Temperature [K]	% coarse to nominal	% fine to nominal
0	288.35	291.11	291.27	0.94	−0.05
0.1	288.42	291.39	291.36	1.01	0.01
0.2	288.42	291.42	291.38	1.02	0.01
0.3	288.43	291.43	291.37	1.02	0.01
0.4	288.43	291.40	291.34	1.01	0.02
0.5	288.44	291.38	291.34	1.00	0.01
0.6	288.44	291.37	291.35	1.00	0.00
0.7	288.43	291.40	291.37	1.01	0.01
0.8	288.41	291.42	291.37	1.03	0.01
0.9	288.35	291.18	291.29	0.97	−0.03

conducting grid independence tests. Negligible effect in the reattachment points was observed for mesh elements greater than 10 million. It was assured that the numerical residuals were in the order of magnitude 10^{-6} and the solution was considered converged as numerical residuals reached the convergence criteria. The solution did not change much after this criterion was achieved.

A grid independence study was undertaken to verify that the solutions generated by the numerical analysis were not dependent on the resolution of the meshes generated. As a result, a coarser mesh of 20 million cells and a finer mesh of 40 million cells were made and had solutions computed from the 4C discharge 15°C BCs. This was compared to the standard 33-million-cell medium-detail mesh used for the rest of the simulations. Tables 2 and 3 show the grid independence data for the temperature and velocity data taken across the width of the outlet. The velocity data is a near match across the coarse-, medium-, and fine-detail meshes, showing that the solution calculated was not dependent on the mesh resolution. The temperature data again shows very high correlation, with the maximum variance between the coarse- and medium-detail mesh being 1.03%. This is far less than the 10% accepted range of error for CFD solutions [38], again validating the mesh resolution. Given the difference in computational times for the meshes – approximately 10 hours for the coarse mesh, 12 hours for the medium mesh, and 18 hours for the fine mesh – it was decided that the medium-detail mesh was a good balance between computational time and accuracy.

4. Results and discussion

After the controlled experimental and model development study described in the preceding section, this section explains the results obtained for a particular prismatic lithium-ion battery at

Table 3. Grid independence data for velocity contours.

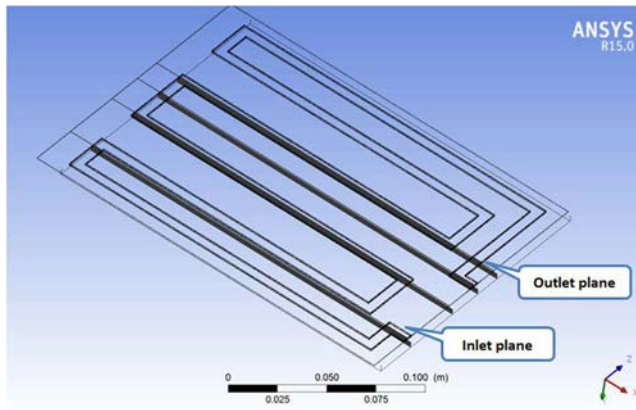| [Data] Chart Count	20 million cells 50% Larger Velocity [m/s]	33 million cells Nominal Velocity [m/s]	40 million cells Next Inlet Channel Finer (0.2 mm) Velocity [m/s]	% coarse to nominal	% fine to nominal
0	0.09	0.01	0.00	30.76	46.15
0.1	0.57	0.57	0.57	1.21	0.17
0.2	0.66	0.66	0.66	0.15	0.60
0.3	0.72	0.72	0.72	0.27	−0.13
0.4	0.76	0.76	0.76	0.13	−0.13
0.5	0.77	0.78	0.77	0.12	0.25
0.6	0.78	0.78	0.78	−0.12	0
0.7	0.78	0.78	0.78	0.63	0
0.8	0.76	0.76	0.76	1.04	0
0.9	0.04	0.01	0.01	−152.63	21.05

**Figure 4.** Vertical planes 1, 2 3, 4 (1 is inlet and 4 is outlet).

different discharge rates (3C and 4C) for the water cooling (BCs of 5°C, 15°C, and 25°C) method.

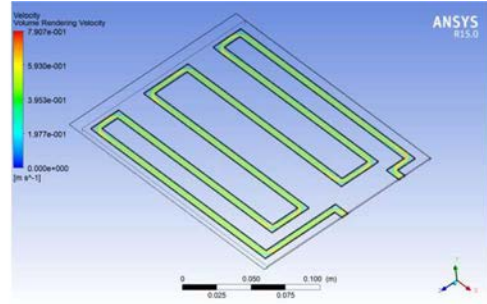### 4.1. Temperature and velocity contours at 3C discharge and 5°C, 15°C, and 25°C BC

Figure 5*a*–5*c* shows the temperature contours as obtained through the numerical study at 3C discharge rate and 5°C, 15°C, and 25°C BC (water cooling method). These contours were obtained at Plane 1 and Plane 4 (planes are shown in Figure 4) of the cooling plate. It should be noted that 10 thermocouples were located on the principal surface of the battery: three were placed near electrodes, three were placed at the center of the battery, two were placed between the top and the middle of the battery, one was placed at the bottom of the battery, and one was located between the center and the bottom of the battery. It is observed that there is a great impact of BC on the performance of battery as well as the circulating water inside the cold plates and it is observed that as the BC increases between 5°C and 25°C for a particular discharge rate of 3C, the temperature contour values also increase. The general cooling patterns are the same, showing greater temperature differences at the inlet of the cooling plate when the water is the coldest. The temperatures vary with the inlet temperature BC, but the overall pattern remains roughly the same. The cooling patterns follow what is seen on the batteries experimentally, with the outlet having a higher temperature than the inlet. The velocity contours are identical in all the cases. This is expected, given the low temperatures involved in the simulations that would have little to no effect on the density of the water. Table 4 provides the summary of water inlet and outlet temperature at 3C discharge rates and different BCs of 5°C, 15°C, and 25°C. The corresponding velocity contours at 3C discharge rate and 5°C, 15°C, and 25°C BC appear in Figure 5*d*–5*f*.

4.2. Temperature and velocity contours at 4C discharge and 5°C, 15°C, and 25°C BC

Figure 6*a*–6*c* shows the temperature contours at 4C discharge rate and 5°C, 15°C, and 25°C BC. These contours were obtained at Plane 1 and Plane 4 (planes are shown in Figure 4) of the cooling plate. It is observed that as the battery discharges, the circulating water in the cold plates gets heated. As the discharge rate increases from 3C to 4C, there is an increase in temperature values as well. The trend observed is that increased discharge rates and increased BCs result in increased temperatures in the cold plate. Table 4 provides the summary of water inlet and outlet temperatures at 4C discharge rates and different BCs of 5°C, 15°C, and 25°C. Again, the general cooling patterns are the same, similar to the results in Section 4.1. There are greater temperature
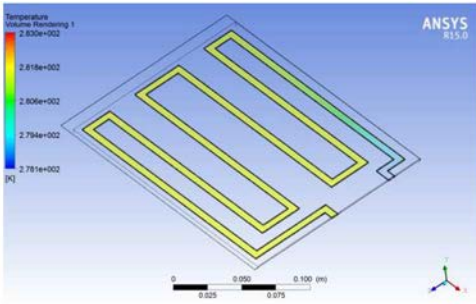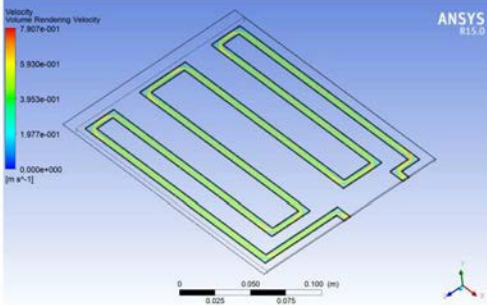
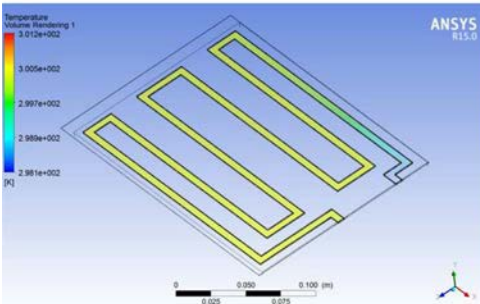(a) Temperature contour at 3C discharge & 5 °C BC

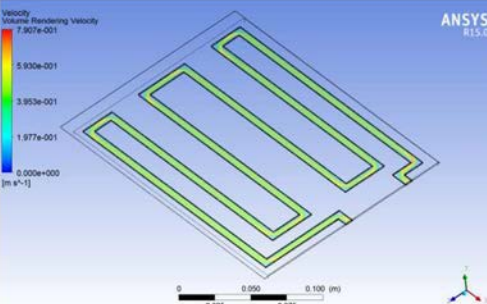(d) Velocity contour at 3C discharge & 5 °C BC
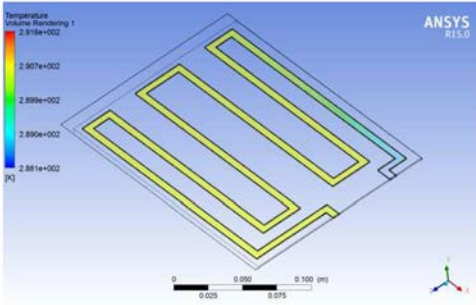
(b) Temperature contour at 3C discharge & 15 °C BC

(e) Velocity contour at 3C discharge & 15 °C BC

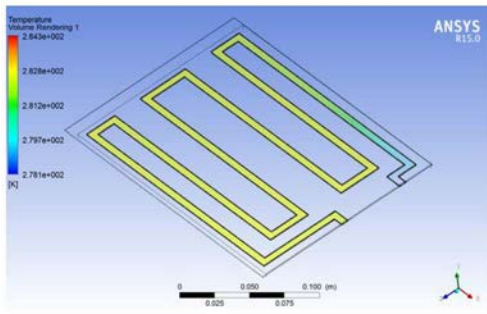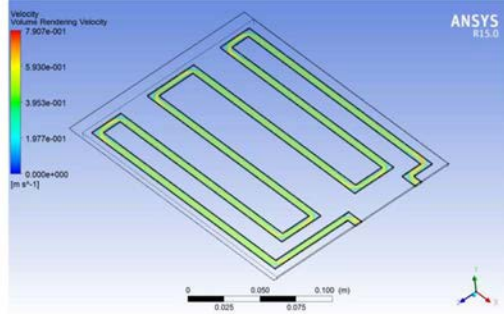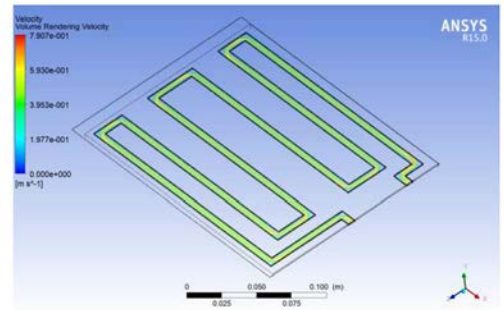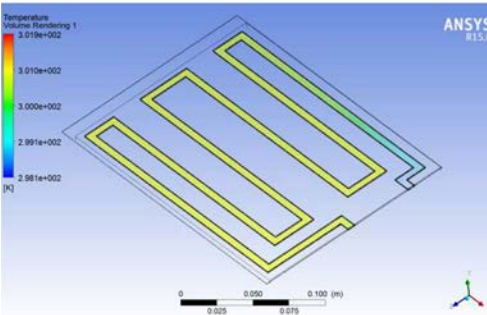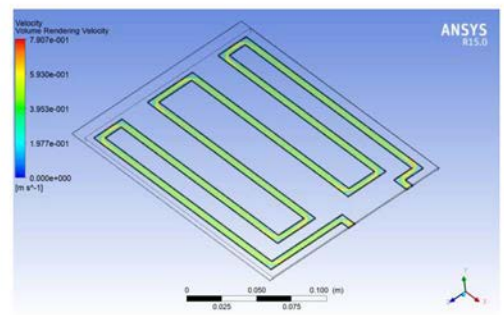(c) Temperature contour at 3C discharge & 25 °C BC

(f) Velocity contour at 3C discharge & 25 °C BC

Figure 5. Temperature and velocity contours at 3C discharge and 5°C, 15°C, and 25°C BC.

differences at the inlet of the cooling plate when the water is the coldest. The temperature values vary with the inlet temperature BC, but the overall pattern remains roughly the same. Likewise, the velocity contours are the same in all the cases. Figure 6d–6f shows the corresponding velocity contours at 4C discharge rate and 5°C, 15°C, and 25°C BC.

Table 4. Summary of water inlet and outlet temperature at 3C and 4C discharge rates and different boundary conditions.

| | | Water inlet and outlet temperature [K] | | | |
| | | 3C | | 4C | |
Cooling type	Boundary condition [°C]	Inlet	Outlet	Inlet	Outlet
Water cooling	5	278.15	283.05	278.15	284.31
	15	288.15	291.60	288.15	292.81
	25	298.10	301.21	298.10	301.91

(a) Temperature contour at 4C discharge & 5 °C BC

(d) Velocity contour at 4C discharge & 5 °C BC
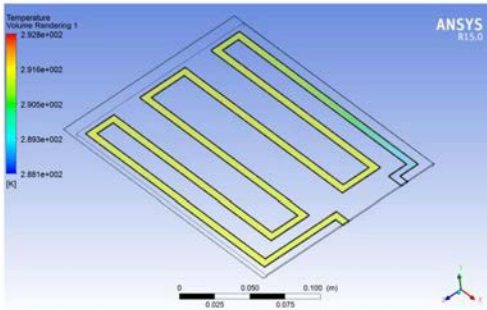
(b) Temperature contour at 4C discharge & 15 °C BC

(e) Velocity contour at 4C discharge & 15 °C BC

(c) Temperature contour at 4C discharge & 25 °C BC

(f) Velocity contour at 4C discharge & 25 °C BC

Figure 6. Temperature and velocity contours at 4C discharge and 5℃, 15℃, and 25℃ BC.

5. Conclusions

This paper presented a comparative study of the temperature and velocity distributions within the minichannel cold plates placed in a prismatic lithium-ion battery cell. The study was conducted both experimentally, and numerically using the RANS models in ANSYS Fluent. The discharge rates of 3C and 4C, and boundary conditions of 5°C, 15°C, and 25°C were investigated. It was found that the temperature distributions within minichannel cold plates increased as the C-rates increased. It was also observed that the increased discharge rates (between 3C and 4C) and increased operating temperature (between 5°C, 15°C, and 25°C) resulted in the increased temperatures measured at 10 distributed locations on the battery surface. The cooling patterns from the numerical results are consistent with those obtained experimentally. Lastly, it was also found that the thermocouple sensors closest to the electrodes provided higher temperatures than the centerline-thermocouple sensors.

These results provide useful new information for the design and optimization of battery cooling systems.

References

[1] Q. Wang, Q. Sun, P. Ping, X. Zhao, J. Sun, and Z. Lin, Heat Transfer in the Dynamic Cycling of Lithium–Titanate Batteries, *Int. J. Heat Mass Transfer*, vol. 93, pp. 896–905, 2016.

[2] Z. Ling, F. Wang, X. Fang, X. Gao, and Z. Zhang, A Hybrid Thermal Management System for Lithium Ion Batteries Combining Phase Change Materials with Forced-Air Cooling, *Appl. Energy*, vol. 148, pp. 403–409, 2015.

[3] H. Ge, J. Huang, J. Zhang, and Z. Li, Temperature-Adaptive Alternating Current Preheating of Lithium-Ion Batteries with Lithium Deposition Prevention, *J. Electrochem. Soc.*, vol. 163, no. 2, pp. A290–A299, 2016.

[4] A. Ritchie and W. Howard, Recent Developments and Likely Advances in Lithium-Ion Batteries, *J. Power Sourc.*, vol. 162, pp. 809–812, 2006.

[5] Y. Ye, L. H. Saw, Y. Shi, and A. A. Tay, Numerical Analyses on Optimizing a Heat Pipe Thermal Management System for Lithium-Ion Batteries During Fast Charging, *Appl. Therm. Eng*, vol. 86, pp. 281–291, 2015.

[6] C. Alaoui, Solid-State Thermal Management for Lithium-Ion EV Batteries, *Veh. Technol., IEEE Trans.*, vol. 62, no. 1, pp. 98–107, 2013.

[7] Z. Rao, Y. Huo, and X. Liu, Experimental Study of an OHP-Cooled Thermal Management System for Electric Vehicle Power Battery, *Exp. Therm. Fluid Sci.*, vol. 57, pp. 20–26, 2014.

[8] C. H. Wang, T. Lin, J. T. Huang, and Z. H. Rao, Temperature Response of a High Power Lithium-Ion Battery Subjected to High Current Discharge, *Mater. Res. Innovations*, vol. 19, pp. 156–160, 2015.

[9] Z. Rao, S. Wang, M. Wu, Z. Lin, and F. Li, Experimental Investigation on Thermal Management of Electric Vehicle Battery with Heat Pipe, *Energy Convers. Manage.*, vol. 65, pp. 92–97, 2013.

[10] H. Teng, Y. Ma, K. Yeow, and M. Thelliez, An Analysis of a Lithium-ion Battery System with Indirect Air Cooling and Warm-Up, *SAE Int. J. Passenger Cars- Mech. Syst.*, vol. 4, no. 3, pp. 1343–1357, 2011.

[11] F. He and L. Ma, Thermal Management in Hybrid Power Systems using Cylindrical and Prismatic Battery Cells, *Heat Transfer Eng.*, vol. 37, no. 6, pp. 581–590, 2016.

[12] I. Bayraktar, Computational Simulation Methods for Vehicle Thermal Management," *Appl. Therm. Eng*, vol. 36, pp. 325–329, 2012.

[13] M. R. Giuliano, A. K. Prasad, and S. G. Advani, Experimental Study of an Air-Cooled Thermal Management System for High Capacity Lithium–Titanate Batteries, *J. Power Sourc.*, vol. 216, pp. 345–352, 2012.

[14] G.-H. Kim, A. Pesaran, and R. Spotnitz, A Three-Dimensional Thermal Abuse Model for Lithium-Ion Cells, *J. Power Sourc.*, vol. 170, no. 2, pp. 476–489, 2007.

[15] M. R. Giuliano, S. G. Advani, and A. K. Prasad, Thermal Analysis and Management of Lithium–Titanate Batteries, *J. Power Sourc.*, vol. 196, no. 15, pp. 6517–6524, 2011.

[16] L. W. Jin, P. S. Lee, X. X. Kong, Y. Fan, and S. K. Chou, Ultra-thin Minichannel LCP for EV Battery Thermal Management, *Appl. Energy*, vol. 113, pp. 1786–1794, 2014.

[17] E. W. Lemmon, and R. T. Jacobsen, Viscosity, and Thermal Conductivity Equations for Nitrogen, Oxygen, Argon, and Air, *Int. J. Thermophys.*, vol. 25, no. 1, pp. 21–69, 2004.

[18] H. Park, A Design of Air Flow Configuration for Cooling Lithium Ion Battery in Hybrid Electric Vehicles, *J. Power Sourc.*, vol. 239, pp. 30–36, 2013.

[19] L. Fan, J. M. Khodadadi, and A. A. Pesaran, A Parametric Study on Thermal Management of an Air-Cooled Lithium-Ion Battery Module for Plug-in Hybrid Electric Vehicles, *J. Power Sourc.*, vol. 238, pp. 301–312, 2013.

[20] Z. Rao and S. Wang, A Review of Power Battery Thermal Energy Management, *Renew. Sustain. Energy Rev.*, vol. 15, no. 9, pp. 4554–4571, 2011.

[21] S. Panchal, I. Dincer, M. Agelin-Chaab, R. Fraser, and M. Fowler, Experimental, and Theoretical Investigation of Temperature Distributions in a Prismatic Lithium-Ion Battery, *Int. J. Therm. Sci.*, vol. 99, pp. 204–212, 2016.

[22] S. Panchal, I. Dincer, M. Agelin-Chaab, R. Fraser, and M. Fowler, Thermal Modeling and Validation of Temperature Distributions in a Prismatic Lithium-Ion Battery at Different Discharge Rates and Varying Boundary Conditions", *Appl. Therm. Eng*, vol. 96, pp. 190–199, 2016.

[23] S. Panchal, I. Dincer, M. Agelin-Chaab, R. Fraser, and M. Fowler, Experimental and Theoretical Investigations of Heat Generation Rates for a Water Cooled LiFePO4 Battery, *Int. J. Heat Mass Transfer*, vol. 101, pp. 1093–1102, 2016.

[24] A. Pruteanu, B. V. Florean, G. Maria Moraru, and R. C. Ciobanu, Development of a Thermal Simulation and Testing Model for a Superior Lithium-Ion-Polymer Battery, *Optimiz. Electr. Electron. Equip (OPTIM), IEEE*, pp. 947–952, 2012.

[25] J. Yi, U. S. Kim, C. B. Shin, T. Han, and S. Park, Three-Dimensional Thermal Modeling of a Lithium-Ion Battery Considering the Combined Effects of the Electrical and Thermal Contact Resistances Between Current Collecting Tab and Lead Wire, *J. Electrochem. Soc.*, vol. 160, no. 3, pp. 437–443, 2013.

[26] X. Hu, S. Asgari, S. Lin, S. Stanton, and W. Lian, A Linear Parameter-Varying Model for HEV/EV Battery Thermal Modeling, *Energy Convers. Congr. Exposit. (ECCE), IEEE*, pp. 1643–1649, 2012.

[27] A. Smyshlyaev, M. Krstic, N. Chaturvedi, J. Ahmed, and A. Kojic, PDE Model for Thermal Dynamics of a Large, *Am. Control. Conf. (ACC), IEEE*, pp. 959–964, 2011.

[28] A. Samba, N. Omar, H. Gualous, Y. Firouz, P. V. d. Bossche, J. V. Mierlo, and T. I. Boubekeur, Development of an Advanced Two-Dimensional Thermal Model for Large size Lithium-ion Pouch Cells, *Electrochim. Acta*, vol. 117, pp. 246–254, 2014.

[29] G. Li and S. Li, Physics-Based CFD Simulation of Lithium-ion Battery under the FUDS Driving Cycle, *ECS Trans.*, vol. 64, no. 33, pp. 1–14, 2015.

[30] P. Vyroubal, T. Kazda, J. Maxa, and J. Vondrák, Analysis of Temperature Field in Lithium Ion Battery by discharging, *ECS Trans.*, vol. 70, no. 1, pp. 269–273, 2015.

[31] K. Yeow, M. Thelliez, H. Teng, and E. Tan, Thermal Analysis of a Li-ion Battery System with Indirect Liquid Cooling Using Finite Element Analysis Approach, *SAE Int. J.*, vol. 1, no. 1, pp. 65–78, 2012.

[32] B. S. Yilbas, M. Khalil Anwar, and S. Z. Shuja, A Mobile Thermal Battery and Thermal Energy Storage Enhancement, *Numer. Heat Transfer, Part A: Appl.*, vol. 69, no. 11, pp. 1297–1309, 2016.

[33] S. Wen, E. Fleming, L. Shi, and A. K. Da Silva, Numerical Optimization and Power Output Control of a Hot Thermal Battery with Phase Change Material, *Numer. Heat Transfer, Part A: Appl.*, vol. 65, no. 9, pp. 825–843, 2014.

[34] Z. Rao, Q. Wang, and C. Huang, Investigation of the Thermal Performance of Phase Change Material/Mini-Channel Coupled Battery Thermal Management System," *Appl. Energy*, vol. 164, pp. 659–669, 2016.

[35] K. R. Anderson, M. Devost, W. Pakdee, and N. Krishnamoorthy, STAR CCM + CFD Simulations of Enhanced Heat Transfer in High-Power Density Electronics Using Forced Air Heat Exchanger and Pumped Fluid Loop Cold Plate Fabricated from High Thermal Conductivity Materials, *J. Electron. Cool. Therm. Control*, vol. 3, pp. 144–154, 2013.

[36] Y. Huo, Z. Rao, X. Liu, and J. Zhao, Investigation of Power Battery Thermal Management by Using Mini-Channel Cold Plate, *Energy Convers. Manage.*, vol. 89, pp. 387–395, 2015.

[37] Inc., ANSYS, ANSYS Fluent Advanced Add-On Modules, ANSYS, Inc., November 2013. [Online]. Available: http://www.ansys.com. [Accessed November 2013].

[38] G. Karniadakis and S. Sherwin *Introduction in Spectral/hp Element Methods for CFD*, 2nd ed., Oxford University Press, New York, USA, 2005.